Electromagnetic excitation of the delta resonance in nuclei

J. S. O'Connell, W. R. Dodge, J. W. Lightbody, Jr., and X. K. Maruyama
National Bureau of Standards, Gaithersburg, Maryland 20899

J. -O. Adler, K. Hansen, and B. Schrøder
University of Lund, Department of Physics, Sölvegatan 14, S-223 62 Lund, Sweden

A. M. Bernstein, K. I. Blomqvist, B. H. Cottman, J. J. Comuzzi, R. A. Miskimen, and B. P. Quinn
Laboratory for Nuclear Science and Department of Physics, Massachusetts Institute of Technology, Cambridge, Massachusetts 02139

J. H. Koch and N. Ohtsuka
National Institute for Nuclear and High-Energy Physics, 1009 DB Amsterdam, The Netherlands
(Received 3 November 1986)

Inclusive cross sections for the proton and nuclear targets of $A=4$, 9, 12, and 16 were measured for 537 and 730 MeV electrons scattered at 37.1 deg. Systematic features of the continuum scattering data are compared with other electron scattering data and with photoabsorption measurements. A model calculation based on the isobar-hole formalism is compared with the data in the delta resonance region.

I. INTRODUCTION

Electromagnetic pion production by a free nucleon for energy transfers between 140 and 500 MeV is dominated by the pion-nucleon resonance at 1232 MeV, the Δ ($T=\frac{3}{2}, J^{\pi}=\frac{3}{2}^{+}$) whose width is 115 MeV. The production on nucleons bound in nuclei is expected to show a variety of medium modifications of mainly the resonant, but also nonresonant production mechanism. This paper reports[1] the results of measurements of inelastic scattering at 37.1° of 537 and 730 MeV incident electrons from five targets ($A=1,4,9,12,16$) in the delta resonance region. Measurements[2-5] of the absorption cross section of photons in the same energy region have also recently been reported. The picture that emerges from these studies suggest that medium modifications of the fundamental electromagnetic absorption process on the nucleon are large, but that all nuclei display the same reaction cross section per nucleon. To further study the effects of the nuclear medium, the present work extends these studies to virtual photons.

The present measurement was made at the Bates Linear Accelerator using a magnetic spectrometer with a focal plane array of wire chambers and a gas Čerenkov detector. The experimental arrangement is described in Sec. II. The data analysis and the conversion of counting rates to cross sections is treated in Sec. III; the necessary radiative corrections are described in Sec. IV. A discussion of the systematic features that emerge from our data is given in Sec. V. A comparison with other electron scattering data and with photoabsorption results is made in Sec. VI. In Sec. VII a calculation based on the isobar-hole formalism is compared to the data in the delta region. At lower excitation energy a Fermi gas model calculation is compared with the measured quasifree peak. Conclusions are drawn in Sec. VIII.

The notation used in this paper is as follows: $(E_1,\mathbf{k}_1)$ and $(E_2,\mathbf{k}_2)$ are the energy and momentum of the incident and scattered electron; θ is the electron scattering angle; $\omega=E_1-E_2$ and $\mathbf{q}=\mathbf{k}_1-\mathbf{k}_2$ are the energy and momentum transferred to the target nucleus; $Q^2=q^2-\omega^2>0$ is the square of the four-momentum transfer.

II. EXPERIMENTAL ARRANGEMENT

The experiment was performed at the Bates Linear Accelerator Center using electrons of 537 and 730 MeV. The isochronous recirculation system was used to transport the electron beam from the single pass output of the Linac back to the input to be reinjected into the accelerator a second time. The design and general operation of the recirculation system[6,7] and the Linac[8,9] have been described elsewhere. The beam energy was measured to an accuracy of 0.5% in this experiment. The electrons were scattered from natural isotopic abundance targets of hydrogen, helium, beryllium, carbon, and beryllium oxide. The hydrogen and helium targets were in the form of gases at 2.07 MPa in a 12.7-cm diameter aluminum cell cooled to liquid nitrogen temperatures. The beryllium, carbon, and beryllium oxide were in the form of solid self-supporting targets of 18.4, 25.5, and 21.5 mg/cm^2, respectively. Electrons scattered at 37.1° were detected using the dispersion matched energy loss spectrometer system.[10,11,12]

The beam charge was measured by a pair of toroids which have been calibrated[10] to an absolute accuracy of 0.1% at peak current. Solid angles were limited to keep the measured detector dead times below 10%. The solid angle acceptance was determined by a pair of slits in front

of the spectrometer and 1.8 m from the target chamber. The height and width of the slit openings were measured to an accuracy of 0.08 mm, corresponding to an uncertainty of 0.8% at the smallest solid angle used in this experiment (0.042 msr). In addition, an independent set of horizontal slits was placed between the solid angle defining slits and the target to mask the spectrometer from electrons scattered from the entrance and exit windows of the gas target cells.

A coincidence requirement was imposed between events detected at a flowing-gas Čerenkov detector and the wire chambers to discriminate against pions. The Čerenkov medium was freon 114 at standard temperature and pressure (STP) which has an index of refraction $n=1.0014$. Under these conditions, the Čerenkov detector has a pion detection threshold of 2.6 GeV/c and an electron threshold of 9.4 MeV/c. The physical design incorporates front-surface mirrors 7.5×30 cm^2, curved in the long dimensions with differing radii of curvature and laid out side by side in an array which approximates a paraboloid. The dimensions and orientation of the system are chosen to accept light emitted by all electrons which pass through the drift chamber system with trajectories close to those prescribed by the spectrometer optics. The light is then focused at the photocathode of a single RCA 8854, 5-in. diameter, 14 stage photomultiplier tube with an uv transmitting window.

The freon gas Čerenkov counter was 98% efficient across the 6% momentum bite of the spectrometer and drift chamber system, except for 1% at the high momentum end where efficiency fell to 93%. This behavior is believed to have resulted from the fact that the Čerenkov interaction length was shorter at the high momentum end of the detector. The inefficiency was determined by measuring spectra at energy losses below pion production threshold. The momentum distribution of those events which triggered a plastic scintillator, but which failed to trigger the Čerenkov counter, compared to the scintillator events alone, reflects the Čerenkov detector inefficiency. The inefficiency was parametrized and a channel-by-channel correction across the focal plane was then applied to each spectrum. The well known values of elastic cross sections for the solid targets when the elastic peaks were located in the inefficient region of the focal plane could be reproduced with this procedure, confirming the adequacy of the correction technique employed.

III. DATA ANALYSIS

For each target a spectrum of counts as a function of energy loss was obtained for final momenta ranging from approximately 100 MeV/c up to the elastic peak. This was done by summing the momentum spectra at each spectrometer setting into several energy-loss bins. The spacing between these settings was approximately equal to the 6% momentum acceptance of the spectrometer, allowing almost continuous spectra to be measured. The central energy of each bin was calculated by using spectrometer constants determined in previous experiments. The incident beam energy was determined from the final energies of elastically scattered electrons. Measurements on targets having greatly differing recoil energies gave consistent values of the incident momentum.

Empty-target count rates were subtracted on a bin-by-bin basis from the count rates of the two gas targets. The contribution from the empty target was almost negligible for an energy loss less than 0.6 E_1 but grew rapidly beyond this point, becoming a 20—30% effect at 75% energy loss. At large inelasticities the distribution of events in the direction transverse to the bend plane of the spectrometer was found to have a flat background component in addition to the distribution predicted from the known slit geometry and spectrometer optics. This background, which likely resulted from neutron-induced charged particles, was subtracted from the data. Its contribution was determined by making a two parameter fit of the data, assumed to be the sum of the expected distribution and a flat background. This correction was only about 10% even at the lowest final energies presented here. At energy losses greater than about 80% this background and the empty cell contribution grew so large that accurate cross-section determination became impractical. To determine the contribution of pair-produced electrons, measurements were made with the magnetic field of the spectrometer reversed to detect the positrons. For solid targets these positron spectra were subtracted from the corresponding electron spectra. In the case of the gas targets, however, with $Z=1$ and 2, this contribution was calculated to be negligible. The measured pair count rate for gas targets was corrected by the empty target subtraction.

Conversion of count rate to cross section was straightforward in the case of the solid targets as their thickness and the angular acceptance of the spectrometer were known. The ^{16}O data were obtained by subtracting results obtained for BeO and Be targets. The gas target densities were determined by comparing the radiatively corrected count rate in the elastic peak with known elastic cross sections. The helium target was found to have a small contamination of hydrogen which manifested itself by adding a relatively sharp hydrogen peak on the broad helium quasielastic peak. This was corrected by subtracting 7% of the measured hydrogen cross section from the helium spectra at all final momenta.

IV. RADIATIVE CORRECTIONS

Elastic radiation tails were calculated with the computer code ALLRAD,[13] and subtracted from the spectra. Included in this code are contributions from internal bremsstrahlung, external bremsstrahlung, and collisional (straggling) losses. The count rate due to the latter two effects depends on the square of the target thickness t, while that due to internal bremsstrahlung depends linearly on t. The internal bremsstrahlung calculation takes the single hard-photon emission part of the radiative scattering process completely into account. At small energy loss a multiple soft photon correction to the one photon emission process is applied. The soft photon correction reduces the internal bremsstrahlung component by order of a few percent at large energy loss. The t^2 effects for our solid targets were always less than about 5% of the elastic radiation tail. This was not the case for our gas target data. The

gas target walls, although outside the spectrometer acceptance, contributed to the energy loss process. The large cell wall thickness (377 mg/cm^2) compared to the active gas thickness (13.7 and 27.4 mg/cm^2 for $^1H_2$ and ^{4}He, respectively) led to t^2 effects representing more than 50% of the total radiation tail. Indeed the large resultant radiation tail at large energy loss was the limiting factor, particularly so for the gas cell data, in determining to what energy loss we could reliably subtract the tail. For the gas target at the peak of the Δ the subtraction was as large as 20%, and grew to 80% at the maximum energy loss considered.

In order to calculate the radiation tail for the elastic peak, the form factors for elastic scattering are needed as input data. These must be provided over a q range extending to roughly twice the elastic momentum transfer. This is necessary because electrons can actually be scattered at substantially larger angles and, through recoil involved in the hard photon emission process, emerge at the nominal scattering angle. For the present kinematics, this means that elastic form factors must be specified out to a momentum transfer of 6 fm^{-1}. Below $q=0.3$ fm^{-1} the expression $F=F_0\exp(-q_{\rm eff}^2/q_0^2)$ was used for the form factors. The value of F_0 was obtained from the second Born approximation[14] and $q_0^2=6/R^2$, where R is the root-mean-square (rms) nuclear charge radius and the effective momentum transfer ($q_{\rm eff}$) is given by $q(1+1.16Z\alpha/E_0R)$.

The dipole form factor (with $a=855$ MeV/c) was used for the proton charge form factor and the scaling assumption ($F_M=F_C$) applied in order to include the effects of magnetic scattering. For ^{4}He, experimental form factors[18] were used for $q>0.3$ fm^{-1} (see Refs. 15–17). For ^{9}Be, experimental form factors[18] were used for $q>1$ fm^{-1}. In the range 0.3–1 fm^{-1}, form factors were calculated with the HEINEL distorted-wave Born approximation (DWBA) phase shift code[19] with charge distributions obtained from de Jager *et al.*[20] Similar calculations were performed for ^{12}C and ^{16}O to complement data[21] above $q=1$ fm^{-1}. The radiatively uncorrected differential cross section for ^{12}C at 730 MeV is shown in Fig. 1. Also shown is the calculated radiative tail from the elastic peak, with no renormalization to fit the data at large energy loss. In the delta region the tail is roughly 20% of the total cross section for our gas targets (^{1}H,^{4}He) and 5% for the solid targets (Be, BeO, C).

After subtraction of the elastic radiation tail, radiative and straggling processes were unfolded from the continuum parts of the scattering cross sections in order to obtain the pure nonradiative (radiation and straggling free) electron-nucleus inelastic scattering cross sections.[22] The unfolding procedure begins by making a multinode spline fit to the data. Based on this fit, the data are restructured into equal width bins with a central value and uncertainty appropriately determined from the form of the spline fit. If one of the bins contains no experimental data, a central cross section value equal to the spline fit value is assigned in order to take actual radiative contributions from this bin properly into account. Following this rebinning, we begin the unfolding procedure with bin (i), corresponding to the lowest electron energy loss. We perform radiative

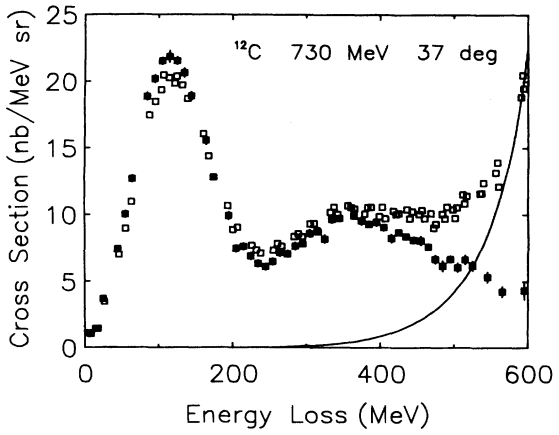

FIG. 1. Cross sections for scattering of 730 MeV electrons from ^{12}C at 37°. The open squares (□) are data not corrected for any radiation effects. The solid squares (■) are obtained by subtracting the elastic radiation tail (solid line) from the data and then performing radiative corrections on the difference.

corrections to the integrated cross section for that bin (assuming a cutoff energy given by half the bin width) and then calculate the corresponding peaking approximation radiation tail[23] (including t^2 effects). The tail cross section in each higher energy loss bin ($j>i$) is then computed and subtracted from the experimental cross section in that bin. We then proceeded to bin ($i+1$), repeat the radiative correction and tail subtraction procedure, iterating until the last bin has been radiatively corrected. The only difficulty in this procedure is the need to know the q dependence of the inelastic form factor for each bin at lower momentum transfers in order to calculate the part of the radiation tail process corresponding to emission of a hard photon, E_γ, followed by inelastic scattering at the lower incident energy E_0-E_γ at the same scattering angle. For lack of experimental data at these lower momentum transfers, we have adopted a phenomenological model to describe the nuclear response function. The model is a relativistic Fermi gas model for the quasifree (QF) knockout peak and a semiphenomenological Δ production model based on a Breit-Wigner line shape, which describes both the known photoproduction data and the observed q dependence. It is well known that such models fail to reproduce the response function in the so-called "dip region" between QF and Δ peaks. To patch up this shortcoming we have introduced a phenomenological peak to account for the additional strength in the dip region. This peak is characterized by a strength, width, and threshold. The functional Q^2 dependence is taken from the transverse part of the relativistic Fermi gas model.[24] This form factor follows that extracted from the data (see Fig. 8). The peak parameters were adjusted to fit our 730 MeV data. This parametrization also describes our 537 MeV data reasonably well. It is important here to recognize that we are performing relatively small corrections, typically 10%, to the continuum region. Within our procedure, if we describe the raw data to within 10–15%,

this translates into a 1—2 % uncertainty into the corrected data. Similarly, although the relativistic Fermi gas model does not do very well in describing the cross sections at the very low energy-loss side of the QF peak, due to the small magnitude of the cross section in this region this contributes negligibly (via straggling and radiation) to the observed large energy-loss cross section. The cross section after corrections for all radiative and straggling processes is shown in Fig. 1 for ^{12}C at an incident electron energy of 730 MeV.

V. CROSS SECTIONS

The radiatively corrected differential (e,e′) cross sections versus electron energy loss for ^{1}H, ^{4}He, ^{9}Be, ^{12}C, and ^{16}O are shown in Figs. 2 and 3, for a scattering angle of 37.1° and incident energies of 730 and 537 MeV, respectively. The elastic peaks are not shown. We do not show results for the gas targets at the lower energy because of difficulties in reliably subtracting the radiation tails when the subtraction exceeds 50% of the data.

Since the momentum transfers far exceed the average internal momenta of nucleons and since the energy transfers necessary to excite the 3-3 resonance far exceed that to eject nucleons, we anticipate that the general features of the nuclear response will be dominated by quasifree processes. This notion is supported by the appearance of the QF and Δ peaks at approximately the energy loss for elastic e-N scattering and Δ production from unbound nucleons, and by the universality of the response functions. This universality can clearly be seen in Figs. 4 and 5, where we have plotted the cross section per nucleon. We will now discuss the general features in more detail.

The quasifree knockout peak is broadened due to Fermi motion. The Δ-production peaks for $A=4,9,12$, and 16 are also broadened but their widths are difficult to estimate. From the 730 MeV data it is clear that there are differences in shape of the QF peaks for the various nuclei, helium having the narrowest width, and the widths increasing with increasing A. This indicates a significantly lower Fermi momentum for helium than for the heavier systems, consistent with the same trend established in earlier Stanford measurements of Moniz *et al.*[25] We can understand the heights of the quasifree cross sections in Figs. 4 and 5 since the area under the peaks is essentially the same; thus the peak cross section per nucleon is inversely proportional to the width. Table I shows our estimated QF and Δ peak positions, peak widths, and peak cross sections for the present data. Also shown in this table are the so-called "average separation energies," $\bar{\epsilon}$, defined as the energy loss at the QF peak minus the kinetic energy of a nucleon (average mass 938.9 MeV) with three-momentum equal to q.

The value of $\bar{\epsilon}$ derived from our ^{4}He data is 6 MeV. This is much smaller than the known 16 MeV single-nucleon separation energy for nuclear matter and the known single-nucleon separation energy for ^{4}He at roughly 20 MeV. The 6 MeV value is, however, consistent with a recent work from Kharkov[26] in which $\bar{\epsilon}$ for ^{4}He was measured as a function of q^2. There is clear evidence in

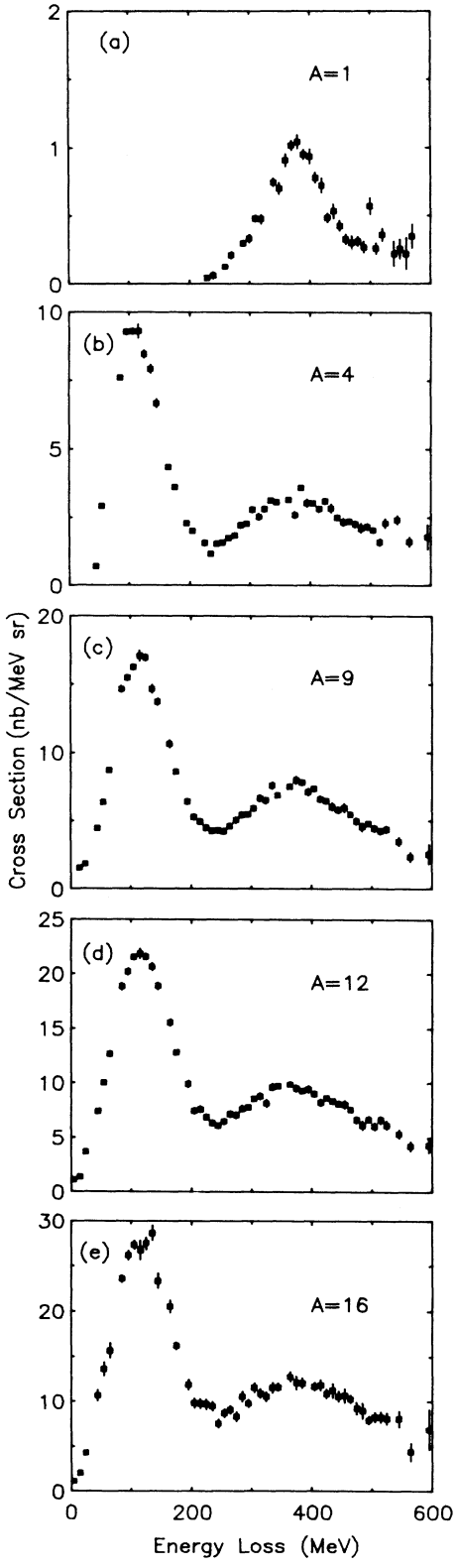

FIG. 2. Final (e,e′) cross sections for $A=1,4,9,12,16$ obtained with 730 MeV incident electrons at a scattering angle of 37.1°. The energy loss is relative to the primary beam energy.

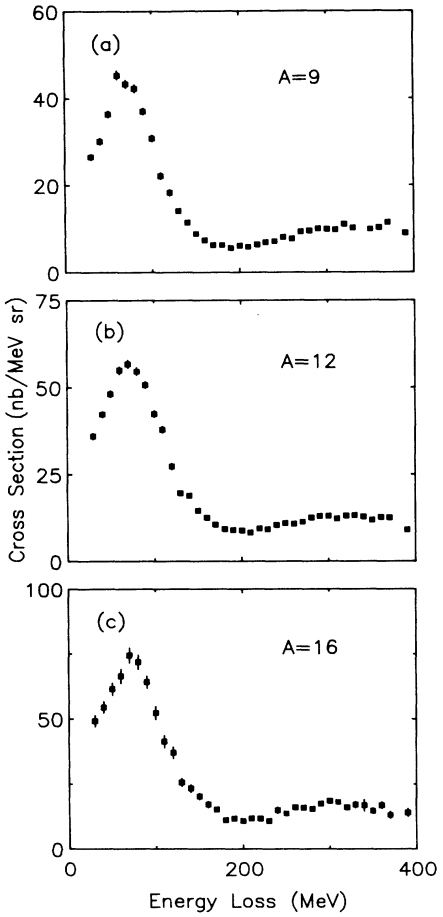

FIG. 3. Final (e,e') cross sections for $A=9,12,16$ obtained with 537 MeV electrons at a scattering angle of 37.1°.

that data that $\bar{\epsilon}$ is not constant and has a minimum value near $|q|=2k_F$. Our results for the p-shell nuclei ($A=9$, 12, and 16) yield a mean value for $\bar{\epsilon}$ of 17 ± 3 MeV. This is only marginally below the result of Moniz *et al.* for ^{12}C of 25 ± 3 MeV. Analysis of the Saclay ^{12}C data of Barreau *et al.*,[27] covering a momentum transfer range from 300 to 550 MeV/c, reveals the same dependence of $\bar{\epsilon}$ on q^2 as seen in ^{4}He and these data are more consistent with the present $\bar{\epsilon}$ results for the $A=9$, 12, and 16 nuclei. The q^2 dependence of $\bar{\epsilon}$ may be an artifact of the oversimplified Fermi gas model for single nuclear knockout; or, it may indicate that another process, such as two-nucleon knockout [meson exchange current (MEC) effect], is competing with the single nucleon knockout process and altering the perceived quasifree peak location.

Turning to the Δ peak, we see that the resonant structure is broader [full width at half maximum (FWHM) ~250 MeV] than the QF peak (FWHM ~100–120 MeV), and also that the shapes for all the nuclei we have looked at are the same. It is plausible that the Δ-production peak for free nucleons (FWHM ~115 MeV) is different from that for bound nucleons because of Fermi motion, Pauli blocking, and coupling of the Δ to

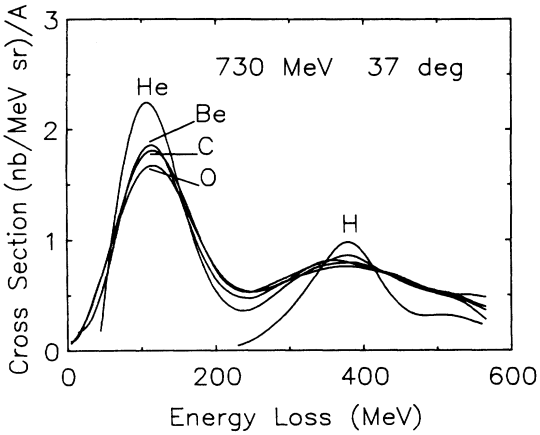

FIG. 4. Fitted (e,e') cross sections per nucleon for $A=1,4,9,12,16$ at 730 MeV at 37°. The curves represent multinode spline fits to the radiatively corrected data.

other than πN decay channels. What is perceived as the Δ resonance in our data is clearly broadened by an additional width of 185 MeV (in quadrature) beyond the natural Δ decay width (115 MeV) and Fermi motion (120 MeV) compared to the free proton peak. While for the QF peak there is a clear shift of the peak to higher energy loss with increasing A, there is no evidence for such a shift in the Δ peak; indeed, there is a hint that the peak shifts to lower energy loss relative to the free proton Δ peak. The quality of our data for the Δ peak is not as good as for the quasifree peak, largely because the apparent peak is so much broader, and does not support similar conjectures.

We have addressed the major features of the response functions, however, there remains the interesting region between the QF and Δ peaks. Within the Fermi gas model, the one-body contributions from quasifree nucleon knockout and Δ excitation have sharp cutoffs in energy transfer due to the assumed kinematics and the ground-

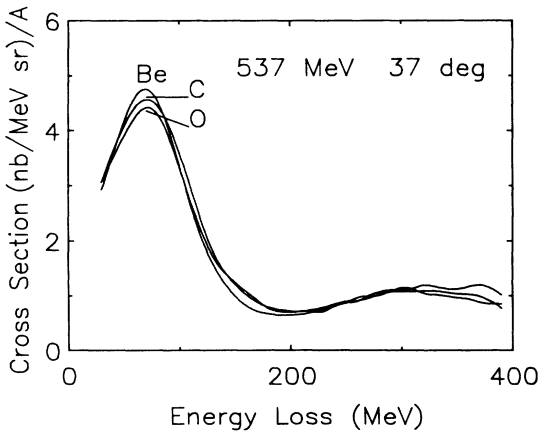

FIG. 5. Fitted (e,e') cross sections per nucleon for $A=9,12,16$ at 537 MeV at 37°. The curves represent multinode spline fits to the radiatively corrected data.

TABLE I. Location and peak cross section per nucleon for the quasifree and delta peaks in the energy-loss spectrum of 730 and 537 MeV electrons scattered at 37.1°. Also given are the widths (FWHM) and average separation energies for the quasifree peak, and the width of the delta resonance for hydrogen.

Element	ω_{QF} (MeV)	$d^2\sigma(QF)/A$ (nb/MeV sr)	Γ_{QF} (MeV)	$\bar{\epsilon}$ (MeV)	ω_Δ (MeV)	$d^2\sigma(\Delta)/A$ (nb/MeV sr)	Γ_Δ (MeV)
^{1}H (537 MeV)	56	a					
(730 MeV)	99	a			380±10	1.03±0.08	120±5
^{4}He (730 MeV)	105±5	2.25±0.14	100±3	6±5	370±10	0.80±0.05	
^{9}Be (537 MeV)	72±3	4.9±0.1	80±5	16±3	315±20	1.11±0.05	
(730 MeV)	115±5	1.91±0.08	115±5	16±5	375±10	0.84±0.04	
^{12}C (537 MeV)	72±3	4.7±0.1	90±5	16±3	315±20	1.06±0.05	
(730 MeV)	115±5	1.83±0.08	125±5	16±5	360±10	0.80±0.04	
^{16}O(537 MeV)	70±3	4.6±0.2	90±5	14±3	310±15	1.12±0.06	
(730 MeV)	120±5	1.76±0.12	125±5	21±5	375±10	0.77±0.06	

[a]Proton elastic cross section is 426 nb/sr at 730 MeV and 1033 nb/sr at 537 MeV.

state momentum distribution. More realistic nuclear models with high-momentum tails will, for example, help to move some of the strength in the quasifree region to higher energy losses and therefore help to fill in the dip region. However, as discussed by Van Orden and Donnelly[24] (and others quoted in Ref. 24), a large part of the dip cross section is thought to be due to two-body effects such as meson exchange currents. This conjecture has been supported by calculations, but typically only half of the observed strength can be explained. From the present data in Figs. 4 and 5, we see that the dip region cross section shows only a weak A dependence; in particular, it does not grow as the number of nucleon pairs as one might expect if the dip cross section were exclusively an effect of long-range correlations. Rather, the insensitivity to A may be due to the s wave, nearest neighbor saturation which occurs at $A=4$. Recent Saclay data[28] for heavier nuclei support this hypothesis.

As discussed earlier the integrated QF peak cross section is essentially given by the sum of the free nucleon cross sections for Z proton and N neutrons. We obtained this result by integrating the quasifree spectrum up to pion threshold ($\omega_{th}=230$ MeV for $E_1=730$ MeV and $\theta_e=37.1°$). Performing the same integral, the Δ peak integrated from ω_{th} to ω_{max} (where $\omega_{max}=550$ MeV for our 730 MeV data) the net areas exceed the free nucleon result by 34%. This excess may be due to mechanisms involving more than one nucleon.

VI. COMPARISON WITH REAL PHOTON RESULTS

A convenient way to compare photoabsorption and inelastic electron scattering data is to write the (e,e′) cross section as

$$\frac{d^2\sigma(e,e')}{d\Omega\, d\omega}=\Gamma_T[\sigma_T(Q^2,\omega)+\epsilon\sigma_L(Q^2,\omega)]\ , \tag{1}$$

where Γ_T is interpreted as the flux of virtual transverse photons striking the nucleus,

$$\Gamma_T=\frac{\alpha}{2\pi^2}\frac{K}{Q^2}\frac{E_2}{E_1}\frac{1}{1-\epsilon}\ , \tag{2}$$

and where K is the equivalent photon energy to produce the same nuclear excitation energy. For quasifree processes

$$K=\omega-\frac{Q^2}{2M}\ . \tag{3}$$

The polarization factor ϵ is the ratio of longitudinal to transverse virtual photons,

$$\epsilon=\left[1+\frac{2q^2}{Q^2}\tan^2\frac{\theta}{2}\right]^{-1}\ . \tag{4}$$

In the limit $Q^2=0$ the quantity σ_T becomes the photon absorption cross section and $\sigma_L\to 0$. Figure 6 shows a plot of $d^2\sigma/\Gamma_T$ vs K for electron and photon data for Be and C. The delta peak occurs at the same equivalent photon energy for both data sets, showing that the absorption is quasifree on the nucleon. The fact that the electron

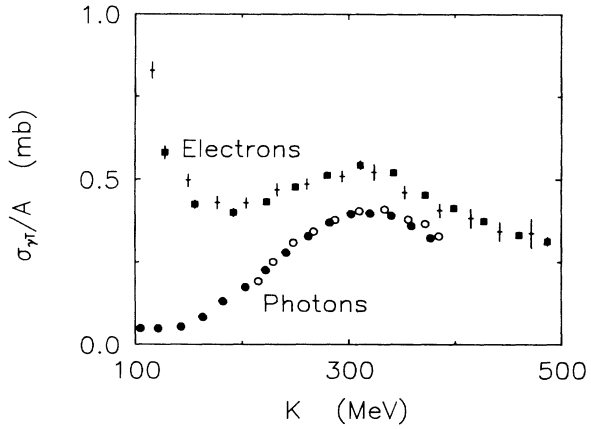

FIG. 6. Equivalent photon cross sections per nucleon, σ_T/A [defined in Eq. (1)], vs equivalent photon energy, K [defined in Eq. (3)]. The solid squares and crosses are the data for ^{12}C and ^{9}Be, respectively. The solid circles and open circles are real photon data for ^{12}C and ^{9}Be, respectively.

data differs from the photon data in the delta region is simply a reflection of the Q^2 dependence of the transition form factor. Other electron scattering data show a very small longitudinal contribution in the delta region. The difference in shape between the electron and photon data is presumably caused by extra absorption mechanisms available to virtual photons because of their higher momentum.

A plot of $d^2\sigma/\Gamma_T$ vs K is also a convenient way to compare (e,e') data at slightly different kinematics because the rapid variation with scattering angle and incident electron energy is removed by dividing each set by Γ_T. In Fig. 6 (e,e') data on carbon from Saclay[27] taken at $E_1=680$ MeV, $\theta=36°$ is plotted with our beryllium data ($E_1=730$ MeV, $\theta=37.1°$). The agreement between these data sets and also between our carbon (plot not shown) and the Saclay carbon measurement gives us confidence as to the absolute normalization of the cross section. A further check is the agreement of our hydrogen data in the delta region with a parametrization of all previous H(e,e') measurements. This is shown in Fig. 7.

It is also of interest to compare the transverse form factors

$$|F_T|^2=\frac{K\sigma_T(Q^2,\omega)}{2\pi^2\alpha} \tag{5}$$

of the delta, dip, and quasifree regions ($K=320$, 140, and 23 MeV, respectively). Figure 8 shows a plot of the carbon transition form factors versus four-momentum transfer. The photon point (Q^2-0) is taken from Ref. 4. Also shown are the transverse form factors (measured in Ref. 27) at the quasifree peak and in the dip region at the threshold for pion production. The photon point for the quasifree process was taken as the peak of the electric dipole giant resonance. The curves all show a rapid rise from the photon point followed by a relatively flat region.

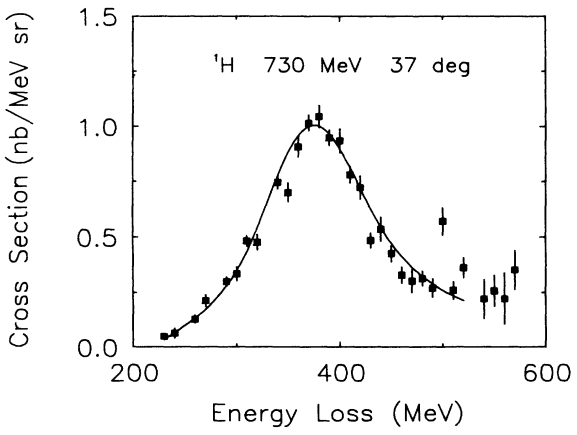

FIG. 7. Cross section for electron scattering from the proton at 730 MeV incident electron energy at a scattering angle of 37°. The curve is derived from a parametrization of previous electron-pion production data.

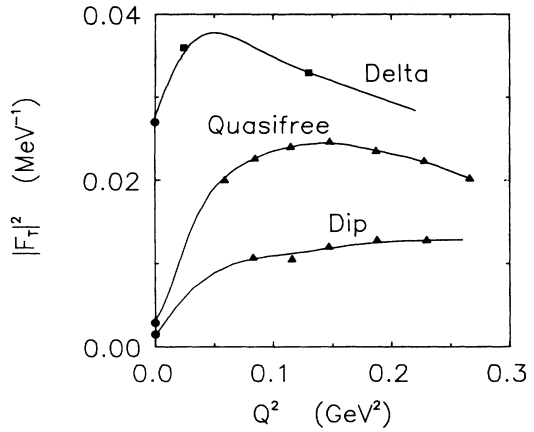

FIG. 8. Carbon transition form factors (■) defined in Eq. (5) vs Q^2 for energy losses corresponding to the peaks at the quasifree and Δ-production cross sections, and the dip region between the two peaks. The solid circles are taken from real photon data (Ref. 4). The solid triangles are taken from Barreau *et al.* (Ref. 27). The curves are to guide the eye.

VII. COMPARISON WITH MODEL CALCULATIONS

The Δ-hole approach has been applied successfully to the description of pion- and photon-induced nuclear reactions in the resonance region. In Ref. 29, this has been extended to inclusive electron scattering. The main emphasis in the Δ-hole approach lies on a careful description of the resonant part of the reaction mechanism. The small nonresonant contributions, which are nearly energy independent, are treated in a simpler way. We outline here only the way the Δ dynamics are treated to calculate the dominant transverse part of the inclusive electron scattering cross section.

To obtain the total absorption cross section σ_T, Eq. (1), the optical theorem is used for the forward elastic scattering cross section for a virtual photon. For scattering proceeding through Δ excitation, this amplitude is written as

$$T_{\gamma\gamma}=\langle 0;\mathbf{q},\omega\,|\,F^{+}_{\gamma N\Delta}G_{\Delta h}F_{\gamma N\Delta}\,|\,0;\mathbf{q},\omega\rangle\ . \tag{6}$$

The initial and final state, consisting of the nuclear ground state and a virtual photon are given by $|0;\mathbf{q},\omega\rangle$. The vertex operator $F_{\gamma N\Delta}$ generates a Δ-hole excitation in this initial state, which propagates inside the nucleus. The dynamical description of Δ propagation is contained in the many-body Green function $G_{\Delta h}$, which has also been used in reactions with pions and real photons:

$$G_{\Delta h}=[D(\omega-H_\Delta)-\delta W-V_{\rm sp}-W_\pi]^{-1}\ . \tag{7}$$

The first part is the free resonance denominator $D(E)=E-E_R+i\Gamma(E)/2$, evaluated at the internal energy available to the Δ. This is done by using the Hamiltonian H_Δ,

$$H_\Delta=T_\Delta+V_\Delta+H_{A-1}\ , \tag{8}$$

where T_Δ is the kinetic energy operator of the Δ and V_Δ is an average binding potential. The operator H_{A-1} takes nucleon binding into account. Since the free resonance denominator $D(E)$ describes the free Δ resonance, cou-

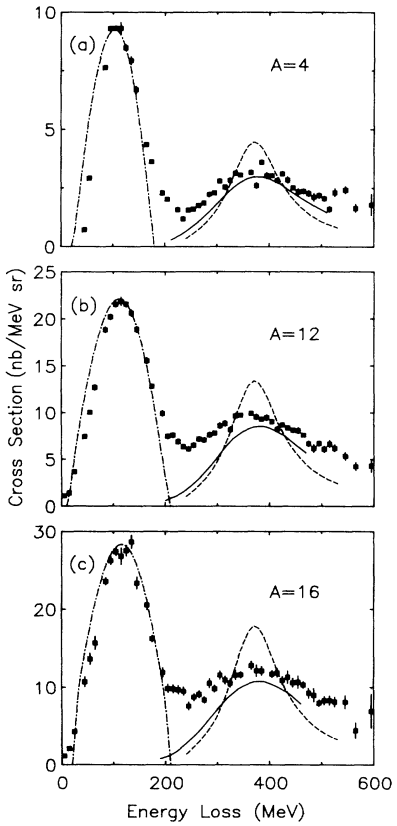

FIG. 9. (e,e') cross sections for $A=4,12,16$ at an incident electron energy of 730 MeV and scattering angle of 37°. The dashed-dotted curve is a relativistic Fermi gas calculation (Ref. 24). The dashed curve is the calculated incoherent sum of cross sections for free nucleons. The solid curve is the full Δ-hole model prediction discussed in the text.

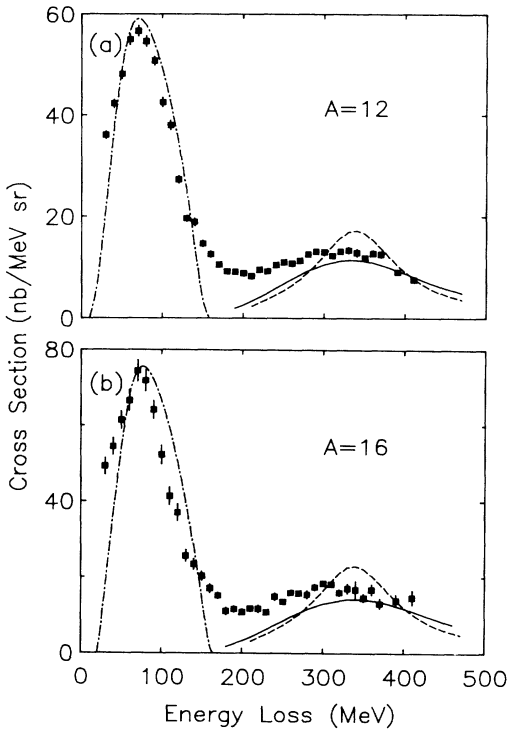

FIG. 10. Same as for Fig. 9 except at an incident electron energy of 537 MeV, and for $A=12$ and 16.

pled to the πN decay channel, one has to take into account that Pauli blocking restricts this decay inside the nucleus. This is included through the operator δW. The term W_π in Eq. (7) describes the coupling of the Δ-hole excitation to a state with a π^0 and the nuclear ground state. While all these contributions can be calculated microscopically in the Δ-hole subspace, the last term, V_{sp}, is a phenomenological parametrization of the coupling to more complicated intermediate channels. The complex strength parameters of this local "spreading potential" were fitted to elastic pion-nucleus scattering data. Its large imaginary part has been interpreted as being mainly due to the coupling to the pion annihilation channel, e.g., $N\Delta \rightarrow NN$.

Results of the Δ-hole calculations are shown in Figs. 9 and 10. By comparing the sum of the free nucleon sections (dashed line) and the full calculation (solid line), we see the effect of the medium modifications. As discussed in Ref. 28, the effects of Pauli blocking (δW) and coupling to the coherent π^0 channel (W_π) tend to cancel. The change in the shape is therefore mainly due to the spreading potential and the Fermi broadening of the resonance. While yielding the observed broad shape of the resonance, the model calculations underestimate the data by an almost constant amount across the resonance. Too little strength is also predicted in the dip region. In the Δ-hole approach, the only coupling to the 2p-2h channel is incorporated through V_{sp} in the resonance propagator. However, as discussed before, there are other ways to reach this channel, such as through meson exchange currents which do not involve the Δ or nucleon knockout followed by a final state interaction. While such effects individually may be small, their interference may be large in the dip region. This has been found by Alberico *et al.*[30]

VIII. CONCLUSIONS

Our main conclusion from this measurement is that the nuclear response in the delta region is nearly the same per nucleon for $A=4$—16. Subsequent measurements at Saclay for $A=40$, 48, and 56 for $E_1=695$ MeV, $\theta=60$ deg confirm this result.[28] This universality in the electromagnetic nucleon response is also seen in photon absorption in the resonance region.

Comparison with predictions of the isobar-hole model show that the main features of the data in the delta region are reproduced, but the magnitude of the cross section falls below the data. We speculate this is due to two (or more) nucleon interaction mechanisms not included in the calculations.

It will be useful to extend our measurements to heavier nuclei and to higher momentum transfers. Coincidence measurements of the decay products in the delta region will also help to further elucidate the mechanism by which electromagnetic radiation is absorbed by a complex nucleus.

[1]J. S. O'Connell *et al.*, Phys. Rev. Lett. **53**, 1627 (1984).
[2]J. Ahrens *et al.*, in *Proceedings of the International Conference on Photopion Nuclear Reactions,* Troy, 1978, edited by P. Stoler (Plenum, New York, 1979), p. 385.
[3]C. Chollet *et al.*, Phys. Lett. **127B**, 331 (1983).
[4]J. Arends *et al.*, Phys. Lett. **98B**, 423 (1981); **146B**, 303 (1984).
[5]J. Ahrens and J. S. O'Connell, Comments Nucl. Part. Phys. **14**, 245 (1985).
[6]J. B. Flanz, S. Kowalski, and C. P. Sargent, IEEE Trans. Nucl. Sci., NS-28, 2847 (1981).
[7]J. B. Flanz and C. P. Sargent, Nucl. Instrum. Methods **241**, 325 (1986).
[8]J. Haimson, in *Linear Accelerators,* edited by P. M. Lapostelle and A. L. Septier (North-Holland, Amsterdam, 1969), Chap. B.3.2, pp. 415—470.
[9]J. Haimson, IEEE Trans. Nucl. Sci., NS-20, 914 (1973).
[10]P. C. Dunn *et al.*, Phys. Rev. C **27**, 71 (1983).
[11]W. Bertozzi *et al.*, Nucl. Instrum. Methods **141**, 457 (1977).
[12]W. Bertozzi *et al.*, Nucl. Instrum. Methods **162**, 211 (1979).
[13]J. Bergstrom, in *Medium Energy Nuclear Physics with Electron Linear Accelerators,* edited by W. Bertozzi and S. Kowalski, (MIT, Cambridge, MA, 1967), Report No. TID-24667.
[14]H. Überall, *Electron Scattering from Complex Nuclei* (Academic, New York, 1971), P. A, p. 50.
[15]J. S. McCarthy, I. Sick, and R. R. Whitney, Phys. Rev. C **15**, 1396 (1977).
[16]R. F. Frosch, J. S. McCarthy, R. E. Rand, and M. R. Yearian, Phys. Rev. **160**, 874 (1967).
[17]R. G. Arnold *et al.*, Phys. Rev. Lett. **40**, 1429 (1978).
[18]R. W. Lourie *et al.*, Phys. Rev. C **28**, 489 (1983).
[19]J. Heisenberg (private communication).
[20]C. W. de Jager, H. de Vries, and C. de Vries, At. Data Nucl. Data Tables **14**, 429 (1974).
[21]I. Sick and J. S. McCarthy, Nucl. Phys. **A150**, 631 (1970).
[22]L. W. Mo and Y. S. Tsai, Rev. Mod. Phys. **41**, 205 (1969).
[23]G. R. Bishop, in *Nuclear Structural Electromagnetic Interactions,* edited by N. MacDonald (Plenum, New York, 1965).
[24]J. W. Van Orden and T. W. Donnelly, Ann. Phys. (N.Y.) **131**, 451 (1981).
[25]E. J. Moniz *et al.*, Phys. Rev. Lett. **26**, 445 (1971).
[26]E. L. Kuplennikov, S. I. Nagornyi, and E. V. Inopin, Yad. Fiz. **41**, 14 (1985) [Sov. J. Nucl. Phys. **41**, 9 (1985)].
[27]P. Barreau *et al.*, Nucl. Phys. **A402**, 515 (1983).
[28]J. Morgenstern (private communication).
[29]J. H. Koch and N. Ohtsuka, Nucl. Phys. **A435**, 765 (1985).
[30]W. M. Alberico, M. Ericson, and A. Molinari, Phys. Lett. **136B**, 307 (1984); Ann. Phys. (N.Y.) **154**, 356 (1984).